

Computation of forces and stresses in solids: Towards accurate structural optimization with auxiliary-field quantum Monte Carlo

Siyuan Chen*

Department of Physics, College of William & Mary, Williamsburg, Virginia 23187, USA

Shiwei Zhang†

*Center for Computational Quantum Physics, Flatiron Institute, New York, New York 10010, USA
and Department of Physics, College of William & Mary, Williamsburg, Virginia 23187, USA*

(Received 22 February 2023; revised 13 May 2023; accepted 17 May 2023; published 26 May 2023)

The accurate computation of forces and other energy derivatives has been a long-standing challenge for quantum Monte Carlo methods. A number of technical obstacles contribute to this challenge. We discuss how these obstacles can be removed with the auxiliary-field quantum Monte Carlo (AFQMC) approach. AFQMC is a general, high-accuracy, many-body total-energy method for molecules and solids. The implementation of back-propagation for pure estimators allows direct calculation of gradients of the energy via the Hellmann-Feynman theorem. A plane-wave basis with norm-conserving pseudopotentials is used for the study of periodic bulk materials. Completeness of the plane-wave basis minimizes the effect of so-called Pulay terms. The ionic pseudopotentials, which can be incorporated in AFQMC in exactly the same manner as in standard independent-electron methods, regulate the force and stress estimators and eliminate any potential divergence of the Monte Carlo variances. The resulting approach allows applications of full geometry optimizations in bulk materials. It also paves the way for many-body computations of the phonon spectrum in solids.

DOI: [10.1103/PhysRevB.107.195150](https://doi.org/10.1103/PhysRevB.107.195150)

I. INTRODUCTION

Interatomic forces and stresses are two important structural properties of a solid-state system. As gradients of the potential energy surface under distortion and deformation, they determine the atomic structure and are crucial for geometry optimizations, molecular dynamics simulations, as well as computations of phonon spectrum and thermodynamic properties, each of which constitutes a large and rich set of applications in physics and materials science.

Density functional theory (DFT) [1–4] has shown incredible success in computing a wide range of physical properties, including interatomic forces and stresses. However, in many materials with stronger electron-correlation effects, computations based on approximate DFT functionals are sometimes not sufficiently accurate to determine structural properties [5,6]. Many methods are being actively pursued which can better describe electron correlations while allowing systematic and realistic calculations to describe molecules and bulk materials.

Quantum Monte Carlo (QMC) methods [7] are one class of such methods, which often show a good balance of accuracy and computational scaling. Indeed QMC methods have seen broad applications in molecules, liquids, and solids, and are one of the primary modern tools for post-DFT calculations in electronic structure. However, while total energies are straightforward to compute and have been the focal point of

QMC methods, computations of observables and correlation functions have been less common with QMC in electronic structure. There have been growing recent efforts to compute properties other than the total energy. Of crucial importance among these are forces and stresses, without which the many-body computations must often rely on DFT (or experiment, if available) predictions of geometry, and thus cannot be truly predictive in many strongly correlated systems. Of course one could compute derivatives by finite difference of the total energy, including the use of correlated sampling [8] and space warp techniques [9,10] for acceleration. However, these have not achieved the desired low computational scaling to allow efficient structural optimization involving many parameters. QMC methods are faced with varying degrees of technical hurdles for direct, systematic computations of forces; to our knowledge no computation of stress tensors has been performed to date.

There are two main forms of QMC methods in electronic structure which have algebraic scaling with system size. The first includes diffusion Monte Carlo (DMC) [11] and the closely related variational Monte Carlo (VMC) [12,13], which treat the first-quantization Hamiltonian working in electron coordinate space. In VMC, the many-body wave function is often explicitly available, so forces and stresses can in principle be computed directly with a modified Hellmann-Feynman estimator [14,15]. This has been applied to structural optimizations [16,17] and estimations of vibrational properties in small molecules [18] and simple solids [19,20]. The accuracy of the computed forces are determined by the quality of the variational wave function. To date the accuracy has not consistently reached such a level as to make VMC by itself a

*schen24@wm.edu

†szhang@flatironinstitute.org

routine post-DFT tool for structural optimization, especially in strongly correlated systems, although this could change with recent developments of more expressive forms of variational ansatz and better optimization techniques, including with neural networks [21–23]. In DMC, the technical hurdles for direct computation of forces and other energy derivatives are more substantial. In principle evaluation of pure estimators by forward walking is required, which has rarely been performed except for light elements [24,25]. Systematic bias in the mixed estimators, as well as statistical divergences, must be dealt with before a general algorithm truly becomes available for structural optimization. (For a more complete discussion of current state of DMC computations of forces, see for example, Ref. [26] and references therein.)

The other form of algebraic-scaling QMC methods in electron structure is phase-free auxiliary-field quantum Monte Carlo (AFQMC) [27,28], which is the focus of the present work. AFQMC works in second-quantization, using random walks of nonorthogonal Slater determinants in orbital space. This formalism provides a nonperturbative, post-DFT method which shares the same Hamiltonian and uses much of the same machinery [29] as in standard electronic structure. The method has had a shorter history of development, but has seen growing applications in lattice models of interacting fermions [30,31], quantum chemistry [32,33], and solid-state physics [34–36]. In a number of recent benchmark studies, AFQMC has demonstrated consistently high accuracy for total energies in both extended systems [37,38] and molecules [39], including large transition metal systems [40]. In addition to total energies, expectation values of other observables that do not commute with Hamiltonian can be computed by a back-propagation (BP) technique [28,41,42]. For molecular systems, computations of forces using a Gaussian basis set have been performed, with geometry optimization on small molecules [43]. In this work we present the computation of forces and stress tensors in AFQMC using planewaves and pseudopotentials, to allow full structural optimization of periodic bulk systems.

The remainder of this paper is organized as follows. In Sec. II, we first briefly review the AFQMC method and the back-propagation technique for the so-called pure estimators to compute observables. We then describe the formulation of the atomic forces and stress tensors within the planewave AFQMC (PW-AFQMC) framework. Section III presents systematic benchmarks of the calculated forces and stresses against explicit computations by finite differences, which validates our method and further illustrates its characteristics. In Sec. IV, we show applications in two different examples of full structural optimization in solids, one a geometry optimization of atomic positions in a fixed supercell using atomic forces, and the other a structural optimization of the cell shape and size using the stress tensors. We then conclude in Sec. V.

II. FORCES AND STRESSES IN PLANE-WAVE AFQMC

A. Basic formalism of AFQMC

AFQMC [27,28] approaches the many-body ground state of a system with imaginary time propagation $\lim_{N \rightarrow \infty} e^{-N\Delta\tau H} |\Psi_T\rangle \rightarrow |\Psi_0\rangle$, where H is the many-body

Hamiltonian whose ground state $|\Psi_0\rangle$ is targeted, $|\Psi_T\rangle$ is a trial wave function that is not orthogonal with $|\Psi_0\rangle$. The propagation is separated into N steps, each of which of imaginary time length $\Delta\tau$, making the propagation an iterative process. The size of the time step $\Delta\tau$ must be chosen to be sufficiently small to minimize commutator errors, known as Trotter errors. The algorithm takes the form of an open-ended random walk, such that there is little restriction on N , which typically takes very large values.

An interacting electronic Hamiltonian, such as the ones in electronic structure under the Born-Oppenheimer approximation, contains one-body and two-body terms. Propagating with the exponential of one-body terms takes a Slater determinant to another Slater determinant [44]. Two-body propagators, which do not preserve the form of a Slater determinant, are treated in AFQMC via the Hubbard-Stratonovich transformation [45,46]:

$$e^{-\frac{\Delta\tau}{2}\lambda\hat{b}^2} = \frac{1}{\sqrt{2\pi}} \int_{-\infty}^{\infty} dx e^{-\frac{1}{2}x^2} e^{x\sqrt{-\Delta\tau}\lambda\hat{b}}. \quad (1)$$

This formula rewrites the propagator of any two-body Hamiltonian term, after it has been expressed in the form of the sum of squares of one-body operators: $H_2 = \sum_i a_i \hat{b}_i^2$, into an integral of one-body propagators. The integral over the auxiliary fields, $\{x_i\}$, can be then evaluated with Monte Carlo.

The iterative process of imaginary time propagation then transforms into a random walk process of a population of Slater determinants (walkers) $\{|\Phi_k^{(n)}\rangle\}$, where n indicates the imaginary-time-step count, and k is an index of the random walker at each time n . Each walker $|\Phi^{(n)}\rangle$ is a Slater determinant propagated from the initial determinant, and is dependent on its specific path history in auxiliary-field (AF) space, $\{\{x_i\}^{(n)}, \{x_i\}^{(n-1)}, \dots, \{x_i\}^{(1)}\}$ (omitting the walker index k). The wave function at each step is represented by a weighted average of all the random walkers at that step, $|\Psi^{(n)}\rangle \propto \sum_k |\Phi_k^{(n)}\rangle / \langle \Psi_T | \Phi_k^{(n)} \rangle$ and it approaches the ground state after a sufficiently large number of steps $n > n_{\text{eq}}$. The value n_{eq} depends on $|\Psi_T\rangle$ and the system, and is such that $n_{\text{eq}}\Delta\tau$ allows the imaginary-time projection from $|\Psi_T\rangle$ to reach $|\Psi_0\rangle$ within the desired statistical accuracy. After convergence, both ensemble and time averages together give a representation of the ground-state wave function, $|\Psi_0\rangle \propto \sum_{n > n_{\text{eq}}} |\Psi^{(n)}\rangle$, whose statistical accuracy can be improved with increasing sample size, following the behavior dictated by the central limit theorem. The actual AFQMC algorithm is augmented by several additional ingredients, including importance sampling (which is embedded in the form of $|\Psi^{(n)}\rangle$ we used above), and the use of a force bias in proposing Monte Carlo moves to improve efficiency [41], as well as the phaseless approximation to control the phase problem [27].

The open-ended random walk scheme yields a form to conveniently evaluate observables that commute with the Hamiltonian, using the *mixed estimator*. For example, the total energy can be computed through

$$\langle H \rangle = E = \frac{\langle \Psi_T | H | \Psi_0 \rangle}{\langle \Psi_T | \Psi_0 \rangle}, \quad (2)$$

for which we only need to propagate one side in the estimator, the ket. The numerator and the denominator can be computed with the random walk averages, and the final estimator for the

energy involves weighted averages of “local energies” of the form $E_L(\Phi_k^{(n)}) = \langle \Psi_T | H | \Phi_k^{(n)} \rangle / \langle \Psi_T | \Phi_k^{(n)} \rangle$.

For observables which do not commute with the Hamiltonian, computations with the mixed estimator in Eq. (2) will incur a bias. A more accurate calculation will require propagation of the bra $\langle \Psi_T |$ to the ground state as well, the so-called *pure estimator*. This is nominally not difficult to achieve. For example, one could sample an entire path of AF for a fixed length of imaginary time with the generalized Metropolis algorithm [47]. However, this approach would cause ergodicity problems when a constraint needs to be imposed along the path to control the sign or phase problem. In the open-ended random walk formulation with importance sampling and constraint, as mentioned above, the projection of the left-side requires the back propagation (BP) scheme [28,41,42] referred to earlier.

We observe that

$$\langle O \rangle \simeq \frac{\langle \Psi_T | e^{-m\Delta\tau H} \hat{O} e^{-n\Delta\tau H} | \Psi_T \rangle}{\langle \Psi_T | e^{-(m+n)\Delta\tau H} | \Psi_T \rangle}, \quad (3)$$

where $\langle O \rangle$ approaches the ground-state expectation as $m, n \rightarrow \infty$. The denominator can be viewed as an overlap of the trial wave function with a propagation of $(m+n)$ steps. If we choose to remember the last m steps of the AFs and propagate $\langle \Psi_T |$ back with the corresponding one-body operators in reverse order, we obtain an estimate of the propagated bra $\langle \Psi_0 | \simeq \langle \Psi_T | e^{-m\Delta\tau H}$. This is the basic idea of BP in AFQMC, which allows a seamless integration of the backward projection with the importance sampling scheme applied in the forward direction. The BP scheme has been applied widely in calculations on lattice models of strong correlations [30,31,48]. An additional bias arises in BP because of the reversal of the direction in which the constraint is applied. Such biases are generally much smaller than the mixed-estimator bias for observables that do not commute with the Hamiltonian, but can be larger than that of the purely variational estimator (which is often hard to compute) [41]. We apply the recently proposed path-restoration technique [42], which can further mitigate the BP bias. Our implementation of the BP scheme in planewave AFQMC is discussed in more detail in Ref. [34]. For the purpose of the present work, the most important aspect to note is that Eq. (3) is reduced to weighted averages of local estimators of the form

$$\langle O \rangle_k^{\text{BP}} \equiv \frac{\langle \bar{\Phi}_k^{(m)} | \hat{O} | \Phi_k^{(n)} \rangle}{\langle \bar{\Phi}_k^{(m)} | \Phi_k^{(n)} \rangle}, \quad (4)$$

where k labels a walker which survives through the $(m+n)$ th step of the random walk, $|\Phi_k^{(n)}\rangle$ is the parent walker of k back in the n th step, and $\langle \bar{\Phi}_k^{(m)} |$ is the back-propagated bra Slater determinant. The weighted average over k yields the Monte Carlo estimate of the expectation value of O given in Eq. (3).

Any one-body operator $O = \sum_{uv} A_{uv} c_u^\dagger c_v$ or two-body operator $O = \sum_{pqrs} V_{pqrs} c_p^\dagger c_q^\dagger c_s c_r$, or their linear combinations, can be computed with the above approach. The estimators $\langle c_u^\dagger c_v \rangle$ and $\langle c_p^\dagger c_q^\dagger c_s c_r \rangle$ are the one-body and two-body reduced density matrices (1rdm, 2rdm) \mathcal{G}_{uv} and \mathcal{G}_{pqrs} , respectively. Computation of $\langle O \rangle$ can therefore be thought of as computing the 1rdm’s and 2rdm’s (which can be obtained via Wick’s theorem [32,49]), and then multiply them with the corresponding

coefficients A_{uv} and V_{pqrs} . This straightforward approach is ineffective with the plane wave basis, where the number of basis functions is much larger than with a localized basis set choice. As such, naive implementations would lead to large storage [$\mathcal{O}(N_{\text{PW}}^2)$ for the 1rdm] and computational costs [$\mathcal{O}(N_{\text{PW}}^3)$ for operations like $\text{Tr}(A_{uv}\mathcal{G}_{uv})$].

Instead, we take a different approach in planewave AFQMC. Recall

$$\mathcal{G}_{uv} = \text{Tr}[(\Phi^\dagger \Psi)^{-1} \Phi^\dagger \mathcal{E}_{uv} \Psi] = [\Psi(\Phi^\dagger \Psi)^{-1} \Phi^\dagger]_{vu}, \quad (5)$$

where Ψ and Φ are the matrix form of the ket and bra Slater determinants, and \mathcal{E} is a matrix with only one nonzero element $\mathcal{E}_{uv} = 1$. We store the intermediate matrix $\Theta = \Psi(\Phi^\dagger \Psi)^{-1}$, which only requires a memory of $\mathcal{O}(N_{\text{PW}} N_e)$. The 1rdm is conveniently restored from Θ and the bra determinant:

$$\mathcal{G}_{uv} = \sum_{t=1}^{N_e} \Theta_{vt}(\Phi^\dagger)_{tu}. \quad (6)$$

The use of fast Fourier transforms (FFTs) and convolutions lead to efficient evaluations. For example, the local part of the electron-ion interaction (see next section for further details):

$$V_{\text{ei}}^L = \sum_{\mathbf{Q} \neq 0} v_{\text{ei}}^L(\mathbf{Q}) \rho(\mathbf{Q}), \quad (7)$$

with $\rho(\mathbf{Q}) \equiv \sum_{\mathbf{G}} c_{\mathbf{G}}^\dagger c_{\mathbf{G}+\mathbf{Q}}$ the “density operator” in \mathbf{Q} -space, is given as

$$\text{Tr}[V_{\text{ei}}^L \mathcal{G}] = \sum_{t=1}^{N_e} \sum_{\mathbf{G}} \Phi_{t\mathbf{G}}^\dagger \sum_{\mathbf{Q}} v_{\text{ei}}^L(\mathbf{Q}) \Theta_{\mathbf{G}+\mathbf{Q},t}, \quad (8)$$

which involves a convolution in the form of $(A \star B)_{\mathbf{q}} = \sum_{\mathbf{p}} A_{\mathbf{p}} B_{\pm\mathbf{p}+\mathbf{q}}$, that is conveniently computed with FFTs and inverse FFTs on the plane-wave grid, and only has a complexity of $\mathcal{O}(N_e N_{\text{PW}} \log N_{\text{PW}})$. The sum on the outer layer also only requires a complexity of $\mathcal{O}(N_e^2 N_{\text{PW}})$.

B. The computation of forces and stresses in planewave AFQMC

With BP and path restoration, pure expectation values of observables can be computed. This allows us to then apply the Hellmann-Feynman (HF) theorem to compute the expectation values of the derivatives of the Hamiltonian directly. Computation of AFQMC forces and stresses are then available, which are given via the HF theorem as expectations of the derivatives of the Hamiltonian.

In the plane-wave basis, the second-quantized Born-Oppenheimer Hamiltonian H can be written as a sum of following components [50]:

$$H = K + V_{\text{ei}} + \gamma_{\text{Ewald}} + V_{\text{ee}}, \quad (9)$$

which are the kinetic energy, the electron-ion interaction (represented by pseudopotentials), the Ewald energy (a system-related constant coming from the interaction of the ions, including with their images due to the periodic cell), and the electron-electron interaction, respectively. A kinetic energy cutoff $|\mathbf{G}|^2 < E_{\text{cut}}$ is imposed on the plane waves, limiting the total number of plane waves to a finite number N_{PW} . The pseudopotential can be separated into local (L) and

nonlocal (NL) components [50]:

$$V_{ei} = \sum_{\mathbf{Q} \neq \mathbf{0}} v_{ei}^L(\mathbf{Q}, \{\vec{\tau}\}) \rho(\mathbf{Q}) + \sum_{\mathbf{G}, \mathbf{G}'} v_{ei}^{NL}(\mathbf{G}, \mathbf{G}', \{\vec{\tau}\}) c_{\mathbf{G}}^\dagger c_{\mathbf{G}'}, \quad (10)$$

where \mathbf{G} and \mathbf{G}' are planewaves within the cutoff E_{cut} , $\mathbf{Q} \equiv \mathbf{G}' - \mathbf{G}$, the operator ρ is the Fourier transform of the real-space electronic density, and $\vec{\tau}$ denotes the positions of ions. We have omitted the spin index in the operators. The electron-electron interaction is $V_{ee} = V^C + N\xi$, where the constant second term (with N being the number of electrons) is similar to the Ewald term from the ions and can be treated together with the latter for convenience, and

$$V^C \equiv \frac{4\pi}{\Omega} \sum_{pqrs} \sum_{\mathbf{Q} \neq \mathbf{0}} \frac{1}{|\mathbf{Q}|^2} c_p^\dagger c_q^\dagger c_s c_r, \quad (11)$$

where each of the indices p, q, r, s denotes a combination of plane-wave vector \mathbf{G} and spin σ . In Eq. (11), momentum conservation $\mathbf{G}_r + \mathbf{G}_s = \mathbf{G}_p + \mathbf{G}_q$ and spin invariance $\sigma_r = \sigma_p, \sigma_q = \sigma_s$ are imposed, and a sum over the spin indices is implicit.

Interatomic forces are derivatives of the total energy with respect to ion positions $\{\vec{\tau}\}$, which are only present in the pseudopotential and ion-ion Ewald energy. From Hellmann-Feynman theorem:

$$F_{ia} = -\frac{\partial E}{\partial \tau_{ia}} = \langle \Psi_0 | -\frac{\partial H}{\partial \tau_{ia}} | \Psi_0 \rangle \equiv \langle \Psi_0 | \hat{F}_{ia} | \Psi_0 \rangle, \quad (12)$$

where i marks each atom and a marks each of the three Cartesian directions. The force observable that will replace \hat{O} in Eq. (4) is therefore written as

$$\hat{\mathbf{F}} = \mathbf{F}_{\text{Ewald}} + \hat{\mathbf{F}}_{ei}, \quad (13)$$

where the Ewald force $\mathbf{F}_{\text{Ewald}}$ is a constant [51]. For the electron-ion contribution, the dependence on ion positions is only in the coefficients v_{ei} , as seen in Eq. (10). The computation of the electron-ion forces therefore requires only a replacement of the coefficients v_{ei} in the total energy computations by $-\partial v_{ei}/\partial \tau_{ia}$. As all dependencies of $\{\vec{\tau}\}$ in v_{ei} are in the form of structure factors (of the form $e^{i\mathbf{G}\cdot\vec{\tau}}$ —see Appendix A), computations of $-\partial v_{ei}/\partial \tau_{ia}$ are straightforward. There is no dependence of the ion positions in the plane-wave basis, hence no Pulay terms from the basis set here.

The stress tensors σ_{ab} are derivatives of total energy with respect to a strain ϵ_{ab} , which describes the deformation \mathbf{U} of any crystal point with respect to its (Cartesian) coordinates \mathbf{X} , $\epsilon_{ab} = \partial U_a / \partial X_b$. The stress tensor is then defined as

$$\sigma_{ab} = -\frac{1}{\Omega} \frac{\partial E}{\partial \epsilon_{ab}}, \quad (14)$$

where Ω is the supercell volume. As the strain tensor is transpose symmetric, so is the stress tensor. Because of statistical errors, this symmetry only holds in a statistical sense in AFQMC. We apply an explicit symmetrization of the stress tensor after the AFQMC calculation: $\bar{\sigma}_{ab} \equiv (\sigma_{ab} + \sigma_{ba})/2$.

Unlike forces, the Hamiltonian terms are not directly dependent on the strain tensor so a chain rule has to be applied through all real-space and reciprocal-space vectors, as well as the lattice volume. This is based on a list of transforms under strain: $\mathbf{r}_a \rightarrow \sum_b (\delta_{ab} + \epsilon_{ab}) \mathbf{r}_b$, $\mathbf{k}_a \rightarrow \sum_b (\delta_{ab} - \epsilon_{ab}) \mathbf{k}_b$, and

$\Omega \rightarrow (1 + \sum_a \epsilon_{aa}) \Omega$, where \mathbf{r} and \mathbf{k} represent, respectively, any real- and reciprocal-space vectors in the Hamiltonian. The observable to evaluate by Eq. (4) is therefore

$$\hat{\sigma}_{ab} = -\frac{1}{\Omega} \left(\sum_{\mathbf{r},c} \delta_{ac} r_b \frac{\partial \hat{H}}{\partial r_c} - \sum_{\mathbf{k},c} \delta_{ac} k_b \frac{\partial \hat{H}}{\partial k_c} + \delta_{ab} \Omega \frac{\partial \hat{H}}{\partial \Omega} \right). \quad (15)$$

Every term in the Hamiltonian in Eq. (9) is affected by the change of the space metric, which means a derivative is needed for each. We write it as

$$\hat{\sigma} = \hat{\sigma}_K + \hat{\sigma}_{ei} + \hat{\sigma}_{\text{Ewald}} + \hat{\sigma}_{ee}. \quad (16)$$

The kinetic and Ewald terms are formally the same as in the corresponding DFT calculations [51]. Dependencies on \mathbf{G} and \mathbf{Q} arise in the electron-ion contribution in Eq. (10), which result in derivatives of the pseudopotential function and the spherical harmonics (see Appendix B for details.) For the electron-electron interaction, the contribution to the stress from the Ewald term is readily available (by setting $Z_i \rightarrow -1, \vec{\tau} \rightarrow \mathbf{0}$ in Ref. [51]). The remaining contribution, from Eq. (11), is

$$\sigma_{ab}^C = \frac{\delta_{ab}}{\Omega} V^C - \frac{8\pi}{\Omega^2} \sum_{pqrs} \sum_{\mathbf{Q} \neq \mathbf{0}} \frac{Q_a Q_b}{|\mathbf{Q}|^4} c_p^\dagger c_q^\dagger c_s c_r, \quad (17)$$

where the second term can be computed similarly to the first term which is already present in the total energy calculation.

We comment on the computational cost of forces and stresses, compared with a total-energy computation. BP is performed occasionally in AFQMC, so it only adds a small additional cost. The computational scaling of BP is also the same as energy computations; in both cases the major cost is in estimating Irdms. The computational scaling for forces and stresses is therefore the same as total-energy-only computations, with an additional prefactor ($\sim 1.2 \times$ in the examples we tested in this work).

C. Sources of errors and their mitigation

At the top level, the formalism we have presented for computing atomic forces and stress tensors have two sources of systematic errors. The first is from the phaseless constraint of AFQMC, which controls the sign or phase problem. In other words, the ground-state wave function sampled from the AFQMC, $|\tilde{\Psi}_0\rangle$, deviates from the exact $|\Psi_0\rangle$. This bias is reflected in the computed total energy (from the mixed estimator), and is generally very small, as seen through many studies and in the large body of benchmark results [37,40]. Additional reduction of the systematic errors can be achieved by better trial wave functions or the use of self-consistent constraints [52].

The other source of error is the BP bias. If $|\tilde{\Psi}_0\rangle$ can be used on both sides to compute a variational estimate of $\langle O \rangle$, then the result is expected to be of a quality consistent with the total energy [41]. However, we cannot do this very efficiently in general, and instead use the BP approach, in which the backward walker paths in Eq. (3) do not satisfy the rigorous constraining sign or gauge condition, which is imposed in the forward-propagating direction [53]. This bias is mitigated

(but not fully suppressed) by the path-restoration scheme, as discussed and illustrated in Ref. [42]. The accuracy of the BP result can still be below that expected from the total energy. One very useful way to quantify this error is via explicit calculations of $\langle O \rangle$, by finite difference using multiple total energy calculations. (This approach has seen many applications in lattice models [31].) The benchmark results below in Sec. III are precisely in this mode, and the excellent agreement between our direct results and the target finite-difference values indicates negligible BP error.

Other sources of errors are present but can be systematically removed. These for example include Trotter errors, population control bias (both of which are also present in total-energy-only calculations), and BP equilibration time bias, all of which can be handled in standard ways [32].

We comment on two other errors which require a bit more attention for forces and especially stress tensors, namely finite-size error and residual basis set error. First, AFQMC computations are performed in finite systems, and the results must be extrapolated to the thermodynamic limit for bulk systems. This applies to the forces and stresses we compute as well. To help reduce finite-size effects, we apply a post-processing correction from a finite-size DFT functional parameterized in Ref. [54] (referred to as KZK in the literature). The KZK finite-size correction is for the total energy. Since forces and stress tensors are both energy derivatives, we can in principle apply a post-processing to them in the same way as to the total energy [54]. However, for the stress tensors, coefficients appearing in the KZK finite-size functional are dependent on the lattice volume, whose derivatives must therefore be accounted for. A simple way to treat this problem and avoiding additional Pulay terms is to use the finite-difference KZK stress $\sigma_{\text{KZK},ab} = -\Delta E_{\text{KZK}}/(\Omega \Delta \epsilon_{ab})$. After that, the usual way of finite-size correction $\sigma_{\text{QMC}}^{\infty} = \sigma_{\text{QMC}}^{\text{FS}} - \sigma_{\text{KZK}} + \sigma_{\text{DFT}}^{\infty}$ can be applied.

The second point worth noting concerns finite basis set errors, or rather the (lack of) balance between the plane wave basis sets in different supercells. As mentioned, the plane-wave basis set, which is independent of ionic positions in the supercell, has essentially no finite basis error for force calculations within a fixed supercell. It does depend on the space metric, and the number of plane waves varies with the supercell size. A Pulay term thus arises for stress tensors. We find this Pulay term to be minimal (“kbar”-level) for a suitable PW cutoff. If a higher accuracy is desired, then common solutions from DFT, such as increasing or smoothing the cutoff [55], can be adopted straightforwardly in PW-AFQMC and works well. An even simpler scheme, in the spirit of KZK, is to correct QMC results with the corresponding DFT cutoff error: $\sigma_{\text{QMC}}^{E_{\text{cut}}=\infty} \approx \sigma_{\text{QMC}}^{E_{\text{cut}}} - \sigma_{\text{DFT}}^{E_{\text{cut}}} + \sigma_{\text{DFT}}^{E_{\text{cut}}=\infty}$. Although approximate, this scheme works well for moderately correlated materials.

III. BENCHMARK AND ILLUSTRATION

To validate our formalism and implementation, and test the accuracy of force and stress computed with PW-AFQMC, we performed a number of benchmark calculations. We compare the forces and stress tensors computed directly by the approach outlined in Sec. II B with the corresponding finite difference results obtained from AFQMC total energies.

The comparison is made in a finite system under identical conditions. The total energy calculations are fully converged with respect to any systematic errors except for the phaseless error, which is expected to be negligibly small in these systems [56]. We ensure that the error from finite difference is smaller than the statistical error in the reference data. Trotter step sizes are extrapolated to zero from three separate finite step-size computations. As discussed in Sec. II C, this comparison thus quantifies all the errors in the forces and stress tensors except that from the phaseless constraint.

We consider a diamond-structured Si in the primitive face-centered cubic (FCC) cell. To benchmark forces, we displace one Si atom along the Cartesian x -axis of the cell. We compare the directly computed forces with the reference result from total energies across a range of displacement, from -1.5% to 1.5% of the experimental lattice constant (10.263 Bohr) with a 0.5% step interval. To obtain the reference data, we compute the total energies with AFQMC across a wider range (-2% to 2% of the lattice constant). We then fit the computed total energy to the quadratic function $E = \frac{1}{2}kx^2 + E_0$. (We have verified that this form is sufficient, as expected for the vicinity of the equilibrium.) The fit is performed in a stochastic way to account for the statistical error bars in the computed total energy: a value is selected randomly at each data point from a Gaussian distribution centered at the mean, with variance given by the Monte Carlo error bar; the set of values for the entire displacement range forms a “sample” which can be fitted to obtain a $\{k, E_0\}$; a large number of samples are used to estimate the value and uncertainty of $\{k, E_0\}$ through the sample average and standard deviation. As a positional derivative of the total energy, the fitted force is then given by $F = -kx$, with statistical uncertainty from the value of k . [This is seen in the linearly growing statistical uncertainty in the reference data in the inset of Fig. 1(a)]. This reference force F_{fit} is then compared with the force directly computed from AFQMC using the algorithm in Sec. II B, F_{direct} . As shown in Fig. 1(a), excellent agreement is seen across the entire range.

To benchmark the computed stress tensors, we proceed in a similar fashion, by deforming the lattice to vary the cell volume and shape, and computing the derivatives of the equation of state to obtain reference data. Here we show an example on the diagonal stress terms, which are associated with lattice volume changes. We use the same silicon structure, varying the lattice constant a around the experimental equilibrium value and calculating the total energy for a range of lattice constants (9.8 to 10.6 Bohr). Similar to the force benchmark, this range is larger than that targeted in the direct stress calculations, to obtain a reliable fit across the range of the benchmark. We then fit the computed equation of state with the Murnaghan equation [57] following the same stochastic procedure described above, and obtain estimates of the the four free parameters $\{E_0, V_0, K_0, K'_0\}$ and their statistical uncertainties. Noting that

$$-\frac{3a}{\Omega} \frac{\partial E}{\partial a} = -\sum_{i=1}^3 \frac{1}{\Omega} \frac{\partial E}{\partial \epsilon_{ii}} = \text{Tr}[\sigma], \quad (18)$$

we can evaluate the strain derivative in the middle by the left-hand side from the Murnaghan equation with the fitted parameters, and compare it with the trace of the directly

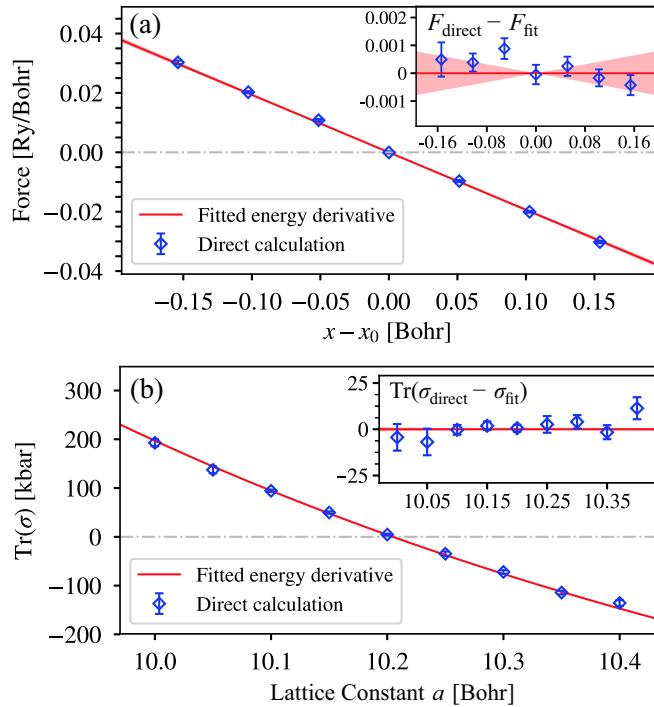


FIG. 1. Benchmark of the computed forces (top panel) and stress tensors (bottom panel) in the Si diamond structure. Forces/stresses directly computed by AFQMC are shown by blue diamonds with error bars, and the reference data, from differentiating the AFQMC total energies, are shown by the red solid curve with error bar as shades. The insets show a zoomed view of the difference between the two. In panel (a) the horizontal axis gives the displacement of one atom along one direction. In panel (b) it is the lattice constant as the cell is varied.

computed stress matrix on the right-hand side. The results are presented in Fig. 1(b). In the main graph, Pulay corrections have been applied to both sets of data. The position in a where either result intercepts 0 shows a small discrepancy from the experimental equilibrium lattice constant. This arises from residual finite-size error (which should vanish when extrapolated to the thermodynamic limit) and has no effect for the purpose here. Excellent agreement is again seen between the computed stress and the benchmark data.

IV. APPLICATIONS IN GEOMETRY OPTIMIZATION

The ability to compute accurate force and stress from AFQMC can potentially enable many applications. One of these is geometry optimization. A full degree-of-freedom (DOF) geometry optimization is possible when we have both forces and stresses available. Interatomic forces allow for optimizations in atom positions, and the stress tensors allow for optimizations of the lattice volume and shape. Here as a first test, we apply these capabilities to two different bulk systems: Si and aluminium nitride (AlN).

The computed forces and stresses can be fed into any optimization routine for structural optimization. Here we use an optimization algorithm that we recently developed [59], called FSSD \times SET (fixed step-size descent with staged error targeting). In a series of tests, in which we emulated forces and

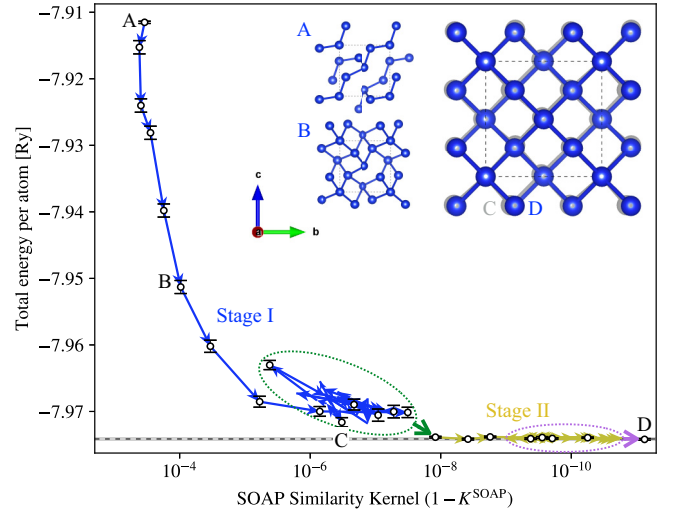


FIG. 2. Optimization of all atomic positions in a supercell of diamond Si. The starting structure (A) is a 50:50 mix of atomic positions in diamond and β -tin structures, placed inside a supercell of equilibrium volume of the diamond structure. The target is the global minimum diamond structure (D). The X axis shows the SOAP similarity kernel [58]. The Y axis shows the AFQMC total energy per Si atom. The scale of statistical uncertainty in the energy is indicated by the error bars at selected steps. The black dashed line shows the energy computed at the target diamond structure, with the gray shades indicating the statistical error. The insets (A–D) show the atomic positions in the y-z plane for four steps along the optimization trajectory, as indicated. Structures (C) and (D) are very close and are shown as overlapping images.

stresses computed from QMC (or any other methods which might contain stochastic noise) by adding synthetic noise to the corresponding DFT results, we studied the efficiency and effectiveness of commonly applied structural optimization algorithms, including some of the latest machine learning optimization methods. We found that the FSSD \times SET approach consistently performed efficiently and robustly under realistic conditions. In the test examples below, we thus apply this algorithm in combination with forces or stresses computed from AFQMC to realize fully *ab initio* many-body structural optimizations.

We first perform a geometry optimization of atomic positions in bulk Si. We consider a cubic supercell with the experimental equilibrium lattice constant of $a = 10.263$ Bohr. The initial positions of the atoms are a 50:50 mix of their fractional coordinates in the diamond structure and the β -tin structure (under strain). Figure 2 illustrates how the system, under PW-AFQMC optimization, transforms into the diamond structure. Arrows connect subsequent steps, and in this optimization run, the SET includes two stages, marked by two different colors. At the beginning of the optimization (the first stage), the total energy drops quickly and in a few steps the atoms change from their initial positions [depicted in Fig. 2(a)] to form a pattern that looks like a distorted diamond structure [Fig. 2(b)]. The structure then converges more slowly in the energy as the atoms move toward the configuration in Fig. 2(c). At this step (step #13), the structure resembles that of the diamond (mean absolute discrepancy of

~ 0.17 Bohr per DOF), and we obtain an AFQMC total energy that is about 1 part in 3100 higher than the global minimum at the diamond structure. Convergence is considered reached at this step for the first stage, and the optimization undergoes a few steps around this converged position, with a position averaging performed among these converged steps [59] to yield a new starting position for the next stage, as indicated by the green oval and arrow. By refining the optimization in a second stage of SET, with smaller targeted statistical error in the AFQMC force computations and a reduced step size in FSSD, we approach the correct minimum diamond structure as depicted in Fig. 2(d). The SOAP similarity kernel [58] ($1 - K^{\text{SOAP}}$) is a measure of how similar the structure is to the target. Our final structure in D has a SOAP similarity kernel difference of 10^{-12} (mean absolute discrepancy of ~ 0.011 Bohr per DOF), and a total energy within one statistical error bar or one part in 106 000 of the energy of the ideal diamond structure.

In the second example, we optimize the lattice volume and shape in solid AlN in the wurtzite structure. Figure 3(a) illustrates the setup. The fractional atomic positions in the cell are fixed to be the values of the wurtzite ($P6_3mc$) structure. The initial structure has a mismatch between the atom positions and the lattice structure, which is tetragonal supercell of a cubic NaCl lattice ($c = 7.64$ Bohr, $a = b = \sqrt{2}c/2$). The target structure, which is the global minimum under ambient condition, is the wurtzite lattice shown on the right. This optimization procedure involves 6 degrees of freedom: the lattice constants (a, b) and the lattice shape ($c/a; \alpha, \beta, \gamma$). We again apply the FSSD \times SET algorithm for the optimization. Instead of the forces as in the example above, this requires repeated computations of the stress tensors with the PW-AFQMC algorithm outlined in the previous section. Figures 3(b)–3(d) demonstrate how the lattice structure transforms toward the global minimum. Convergence of all DOF is seen at step #10 with one stage of FSSD \times SET. The evolution into a final structure of hexagonal wurtzite lattice is evident: c/a increases from $\sqrt{2}$ to ~ 1.60 , and γ changes from 90° to 60° . The averaged lattice parameters after convergence show very good agreement with experimental results.

V. CONCLUSION AND OUTLOOK

We have presented a method for accurate computations of interatomic forces and stress tensors in solid state systems, under the PW-AFQMC framework. The approach is outlined in detail, with a discussion of the sources of errors. Benchmark calculations were performed using accurate total energies to test the formalism and implementation of the direct computation under the Hellmann-Feynman scheme. The approach is then applied in two simple solids as examples, demonstrating fully ab initio structural optimizations of both atomic positions and lattice structures.

The work paves the way for structural optimizations in realistic materials with an accurate many-body method. This opens exciting new opportunities for more predictive computations in correlated materials. A number of questions remain to be further explored to allow systematic applications, including reducing finite-size effects, quantifying the accuracy in strongly correlated materials, improving computa-

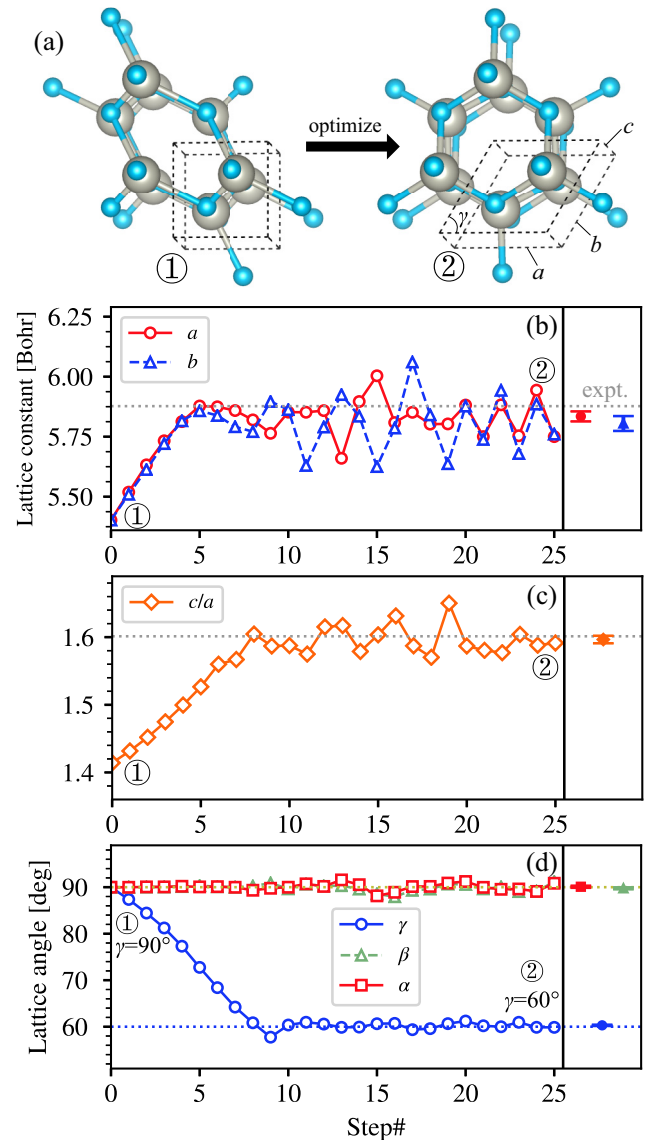


FIG. 3. Optimization of the lattice volume and shape in solid AlN. Panel (a) shows the initial and target structures. Panels (b, c, d) show the lattice constant a, b , the ratio c/a , and the 3 lattice angles α, β, γ , respectively. Convergence is reached at step 10. On the right side of each plot, the average from step 25 is shown with the estimated statistical error bar. Experimental values are shown in dotted lines for comparison.

tional efficiency in our formalism, exploring the BP approach versus automatic differentiation, etc.

Interatomic forces are also key ingredients for computation of the phonon spectrum. The availability of forces from the approach we have presented thus makes possible many-body computation of phonon spectra in solids. A crucial new ingredient which enables systematic phonon calculations is the use of correlated sampling [60], which allows estimates of small differences of systems in proximity, or derivatives by finite-difference. When combined with the approach presented in this work, we can then efficiently compute the derivatives of forces and stresses. A recent improvement of the correlated

sampling algorithm has introduced population control [61], which significantly improves its efficiency and effectiveness.

ACKNOWLEDGMENTS

We are grateful to F. Ma for help and for providing the pseudopotentials used in the present study. We thank H. Krakauer, M. Motta, F. Ma, M. A. Morales, L. K. Wagner, and S. Sorella for useful discussions. S.C. thanks the Center for Computational Quantum Physics, Flatiron Institute for support and hospitality. We also acknowledge support from the U.S. Department of Energy (DOE) under Grant No. DE-SC0001303. The authors thank William & Mary Research Computing and Flatiron Institute Scientific Computing Center for computational resources and technical support. The Flatiron Institute is a division of the Simons Foundation.

APPENDIX A: THE ELECTRON-ION FORCE TERM

We provide some additional details on the differentiation of the pseudopotential coefficients. The local pseudopotential coefficient, v_{ei}^{L} , is given by

$$v_{\text{ei}}^{\text{L}}(\mathbf{Q}) = \frac{1}{\Omega} \sum_i \mathcal{V}_i^{\text{L}}(|\mathbf{Q}|) e^{-i\bar{\tau}_i \cdot \mathbf{Q}}, \quad (\text{A1})$$

where i loops over atoms, $\mathcal{V}^{\text{L}}(Q)$ is a function interpolated from the pseudopotential (we use multiple-projector norm-conserving pseudopotentials) and is the same for atoms of the same species. Differentiating this with respect to an atomic position $\bar{\tau}_\mu$ involves multiplying $i\mathbf{Q}\delta_{i\mu}$ to each term of the sum. Since plane wave AFQMC uses convolutions instead of matrix multiplications, an additional Fourier transform to real space is performed and saved for repeated use.

The nonlocal pseudopotential coefficient, $v_{\text{ei}}^{\text{NL}}$, is given by the Kleinman-Bylander form [62]

$$v_{\text{ei}}^{\text{NL}}(\mathbf{G}, \mathbf{G}') = \sum_J \frac{1}{\eta_J} u_{J,\mathbf{G}}^* u_{J,\mathbf{G}'}, \quad (\text{A2})$$

where J loops over ‘‘projectors’’ and represents a combination of $\{i, l, m\}$, i is the atom number and l, m are the azimuthal and magnetic quantum numbers, η_J is a constant for each J , and

$$u_{J,\mathbf{G}} = \frac{4\pi}{\sqrt{\Omega}} e^{i\bar{\tau}_i \cdot \mathbf{G}^{\mathbf{k}}} \mathcal{V}_J^{\text{NL}}(|\mathbf{G}^{\mathbf{k}}|) Y_{l,m}^*(\mathbf{G}^{\mathbf{k}}), \quad (\text{A3})$$

where $\mathbf{G}^{\mathbf{k}}$ is short hand for $\mathbf{G} + \mathbf{k}$ (\mathbf{k} is the twist angle for a twisted boundary condition). $Y_{l,m}^*$ are *complex-conjugated* spherical harmonics taking the polar coordinates angle (θ, φ) of the input vector.

Differentiating $v_{\text{ei}}^{\text{NL}}$ creates two terms. In each of them, one of the $u_{J,\mathbf{G}}$ is unchanged, while the other will be multiplied by $-i\mathbf{G}^{\mathbf{k}}\delta_{i,\mu}$:

$$-\frac{\partial v_{\text{ei}}^{\text{NL}}(\mathbf{G}, \mathbf{G}')}{\partial \tau_{\mu a}} = \sum_J \frac{i\delta_{i\mu}}{\eta_J} [(u_{J,\mathbf{G}}^* G_a) u_{J,\mathbf{G}'} - u_{J,\mathbf{G}}^* (G'_a u_{J,\mathbf{G}'})], \quad (\text{A4})$$

where $\tau_{\mu a}$ denotes the coordinate in the a -direction of the μ th atom.

Unlike the local electron-ion force, its nonlocal counterpart is not computed with convolutions. However, by writing the pseudopotential in the Kleinman-Bylander form, the dimension has already been drastically reduced. Using the notation U to represent the matrix of $u_{J,\mathbf{G}}$, and \mathcal{U}_a to represent the matrix of $(G_a u_{J,\mathbf{G}})$, we group U^\dagger or \mathcal{U}_a^\dagger with Φ^\dagger , and U or \mathcal{U}_a with Θ , and compute the matrix multiplication within each group first. Sums on J and all electrons are then performed, where $\delta_{i\mu}$ takes effect. In summary, one computes

$$\sum_{t \in \text{electrons}} \sum_J \frac{i\delta_{i\mu}}{\eta_J} [(\mathcal{U}_a \Phi)_{tJ}^\dagger (U \Theta)_{Jt} - (U \Phi)_{tJ}^\dagger (\mathcal{U}_a \Theta)_{Jt}], \quad (\text{A5})$$

where U and \mathcal{U}_a are matrices of dimensions (J, \mathbf{G}) , Θ and Φ are matrices of dimensions (\mathbf{G}, t) .

APPENDIX B: THE ELECTRON-ION STRESS TERM

Based on the formulas in Appendix A, we can also compute the electron-ion contribution to the stress, for which we now have to consider the dependency on $\mathbf{G}, \mathbf{Q}, \Omega$ as well. For the local part:

$$-\frac{1}{\Omega} \frac{\partial v_{\text{ei}}^{\text{L}}(\mathbf{Q})}{\partial \epsilon_{ab}} = \frac{1}{\Omega^2} \sum_i \left[\dot{\mathcal{V}}_i^{\text{L}}(|\mathbf{Q}|) \frac{Q_a Q_b}{|\mathbf{Q}|} + \delta_{ab} \mathcal{V}_i^{\text{L}}(|\mathbf{Q}|) \right] e^{-i\bar{\tau}_i \cdot \mathbf{Q}}, \quad (\text{B1})$$

where $\dot{\mathcal{V}}^{\text{L}}(Q) \equiv d\mathcal{V}^{\text{L}}(Q)/dQ$ is obtained by taking direct derivative of the cubic spline function used for interpolation. This entire object can be pre-computed and used to replace v_{ei}^{L} in the energy computation routine to obtain the local pseudopotential stress contribution. For the nonlocal part,

$$-\frac{1}{\Omega} \frac{\partial v_{\text{ei}}^{\text{NL}}(\mathbf{G}, \mathbf{G}')}{\partial \epsilon_{ab}} = \sum_{J,\mathbf{G},\mathbf{G}'} \frac{1}{\eta_J} [(\bar{u}_{J,\mathbf{G},ab})^* u_{J,\mathbf{G}'} + (u_{J,\mathbf{G}})^* \bar{u}_{J,\mathbf{G}',ab}], \quad (\text{B2})$$

where $\bar{u}_{J,\mathbf{G},ab}$ is a shorthand for $(-1/\Omega)(\partial u_{J,\mathbf{G}}/\partial \epsilon_{ab})$, and contains three terms:

- (1) A contribution from $\Omega^{-1/2}$, which is just $(\delta_{ab}/2\Omega) \times u_{J,\mathbf{G}}$.
- (2) A contribution from the derivative of $\mathcal{V}_J^{\text{NL}}(G)$:

$$\frac{4\pi}{\Omega^{3/2}} e^{i\mathbf{x}_i \cdot \mathbf{G}^{\mathbf{k}}} \frac{G_a G_b}{|\mathbf{G}^{\mathbf{k}}|} [\mathcal{V}'_J(|\mathbf{G}^{\mathbf{k}}|) \cdot Y_{l,m}^*(\mathbf{G}^{\mathbf{k}})]. \quad (\text{B3})$$

- (3) A contribution from the derivative of the spherical harmonics,

$$\frac{4\pi}{\Omega^{3/2}} e^{i\mathbf{x}_i \cdot \mathbf{G}^{\mathbf{k}}} \left[\mathcal{V}_J(|\mathbf{G}^{\mathbf{k}}|) \cdot \frac{\partial Y_{l,m}^*}{\partial G_a^{\mathbf{k}}} G_b^{\mathbf{k}} \right], \quad (\text{B4})$$

which is computed together with the spherical harmonics themselves, and can be obtained with any library that computes $(\partial Y_{l,m}/\partial \theta)$ and $(\partial Y_{l,m}/\partial \varphi)$, with a coordinate transformation from (G, θ, φ) to (G_x, G_y, G_z) .

Written in full, for the nonlocal electron-ion stress, one computes

$$\sum_{t \in \text{electrons}} \sum_J \frac{1}{\eta_J} [(\bar{U}_{ab} \Phi)_{tJ}^\dagger (U \Theta)_{Jt} + (U \Phi)_{tJ}^\dagger (\bar{U}_{ab} \Theta)_{Jt}], \quad (\text{B5})$$

where \bar{U}_{ab} represents the matrix of $\bar{u}_{J,\mathbf{G},ab}$.

- [1] P. Hohenberg and W. Kohn, *Phys. Rev.* **136**, B864 (1964).
- [2] R. O. Jones, *Rev. Mod. Phys.* **87**, 897 (2015).
- [3] A. D. Becke, *J. Chem. Phys.* **140**, 18A301 (2014).
- [4] K. Burke, *J. Chem. Phys.* **136**, 150901 (2012).
- [5] A. P. Gaiduk, F. Gygi, and G. Galli, *J. Phys. Chem. Lett.* **6**, 2902 (2015).
- [6] R. E. Cohen and H. Krakauer, *Phys. Rev. B* **42**, 6416 (1990).
- [7] W. M. C. Foulkes, L. Mitas, R. J. Needs, and G. Rajagopal, *Rev. Mod. Phys.* **73**, 33 (2001).
- [8] J. Shee, S. Zhang, D. R. Reichman, and R. A. Friesner, *J. Chem. Theory Comput.* **13**, 2667 (2017).
- [9] C. Filippi and C. J. Umrigar, *Phys. Rev. B* **61**, R16291 (2000).
- [10] C. J. Umrigar, *Int. J. Quantum Chem.* **36**, 217 (1989).
- [11] P. J. Reynolds, D. M. Ceperley, B. J. Alder, and W. A. Lester, *J. Chem. Phys.* **77**, 5593 (1982).
- [12] W. L. McMillan, *Phys. Rev.* **138**, A442 (1965).
- [13] D. Ceperley, G. V. Chester, and M. H. Kalos, *Phys. Rev. B* **16**, 3081 (1977).
- [14] R. Assaraf and M. Caffarel, *J. Chem. Phys.* **119**, 10536 (2003).
- [15] R. Assaraf and M. Caffarel, *J. Chem. Phys.* **113**, 4028 (2000).
- [16] M. Barborini, S. Sorella, and L. Guidoni, *J. Chem. Theory Comput.* **8**, 1260 (2012).
- [17] R. Guareschi and C. Filippi, *J. Chem. Theory Comput.* **9**, 5513 (2013).
- [18] A. Zen, D. Zhelyazov, and L. Guidoni, *J. Chem. Theory Comput.* **8**, 4204 (2012).
- [19] K. Nakano, T. Morresi, M. Casula, R. Maezono, and S. Sorella, *Phys. Rev. B* **103**, L121110 (2021).
- [20] K. K. Ly and D. M. Ceperley, *J. Chem. Phys.* **156**, 044108 (2022).
- [21] G. Carleo and M. Troyer, *Science* **355**, 602 (2017).
- [22] D. Pfau, J. S. Spencer, A. G. D. G. Matthews, and W. M. C. Foulkes, *Phys. Rev. Res.* **2**, 033429 (2020).
- [23] J. Hermann, Z. Schätzle, and F. Noé, *Nat. Chem.* **12**, 891 (2020).
- [24] S. Chiesa, D. M. Ceperley, and S. Zhang, *Phys. Rev. Lett.* **94**, 036404 (2005).
- [25] A. Badinski and R. J. Needs, *Phys. Rev. E* **76**, 036707 (2007).
- [26] J. Tiihonen, R. C. Clay, and J. T. Krogel, *J. Chem. Phys.* **154**, 204111 (2021).
- [27] S. Zhang and H. Krakauer, *Phys. Rev. Lett.* **90**, 136401 (2003).
- [28] S. Zhang, J. Carlson, and J. E. Gubernatis, *Phys. Rev. B* **55**, 7464 (1997).
- [29] S. Zhang, in *Handbook of Materials Modeling*, edited by W. Andreoni and S. Yip (Springer, Cham, 2018).
- [30] H. Xu, H. Shi, E. Vitali, M. Qin, and S. Zhang, *Phys. Rev. Res.* **4**, 013239 (2022).
- [31] M. Qin, C.-M. Chung, H. Shi, E. Vitali, C. Hubig, U. Schollwöck, S. R. White, and S. Zhang (Simons Collaboration on the Many-Electron Problem), *Phys. Rev. X* **10**, 031016 (2020).
- [32] M. Motta and S. Zhang, *WIREs Comput. Mol. Sci.* **8**, e1364 (2018).
- [33] J. Shee, J. L. Weber, D. R. Reichman, R. A. Friesner, and S. Zhang, *J. Chem. Phys.* **158**, 140901 (2023).
- [34] S. Chen, M. Motta, F. Ma, and S. Zhang, *Phys. Rev. B* **103**, 075138 (2021).
- [35] W. Purwanto, H. Krakauer, and S. Zhang, *Phys. Rev. B* **80**, 214116 (2009).
- [36] F. Ma, W. Purwanto, S. Zhang, and H. Krakauer, *Phys. Rev. Lett.* **114**, 226401 (2015).
- [37] M. Motta, D. M. Ceperley, Garnet Kin-Lic Chan, J. A. Gomez, E. Gull, S. Guo, C. A. Jiménez-Hoyos, T. N. Lan, J. Li, F. Ma, A. J. Millis, N. V. Prokof'ev, U. Ray, G. E. Scuseria, S. Sorella, E. M. Stoudenmire, Q. Sun, I. S. Tupitsyn, S. R. White, D. Zgid, and S. Zhang (Simons Collaboration on the Many-Electron Problem), *Phys. Rev. X* **11**, 029901 (2021).
- [38] M. Motta, C. Genovese, F. Ma, Z.-H. Cui, R. Sawaya, Garnet Kin-Lic Chan, N. Chepiga, P. Helms, C. Jiménez-Hoyos, A. J. Millis, U. Ray, E. Ronca, H. Shi, S. Sorella, E. M. Stoudenmire, S. R. White, and S. Zhang (Simons Collaboration on the Many-Electron Problem), *Phys. Rev. X* **10**, 031058 (2020).
- [39] J. Shee, B. Rudsteyn, E. J. Arthur, S. Zhang, D. R. Reichman, and R. A. Friesner, *J. Chem. Theory Comput.* **15**, 2346 (2019).
- [40] K. T. Williams, Y. Yao, J. Li, L. Chen, H. Shi, M. Motta, C. Niu, U. Ray, S. Guo, R. J. Anderson, J. Li, L. N. Tran, C.-N. Yeh, B. Mussard, S. Sharma, F. Bruneval, M. van Schilfgaarde, G. H. Booth, Garnet Kin-Lic Chan, S. Zhang, E. Gull, D. Zgid, A. Millis, C. J. Umrigar, and L. K. Wagner (Simons Collaboration on the Many-Electron Problem), *Phys. Rev. X* **10**, 011041 (2020).
- [41] W. Purwanto and S. Zhang, *Phys. Rev. E* **70**, 056702 (2004).
- [42] M. Motta and S. Zhang, *J. Chem. Theory Comput.* **13**, 5367 (2017).
- [43] M. Motta and S. Zhang, *J. Chem. Phys.* **148**, 181101 (2018).
- [44] D. Thouless, *Nucl. Phys.* **21**, 225 (1960).
- [45] R. L. Stratonovich, in *Doklady Akademii Nauk*, Vol. 115 (Russian Academy of Sciences, Moscow, 1957), pp. 1097–1100.
- [46] J. Hubbard, *Phys. Rev. Lett.* **3**, 77 (1959).
- [47] S. Zhang, in *Many-Body Methods for Real Materials Modeling and Simulation*, edited by E. Pavarini, E. Koch, and S. Zhang, Vol. 9 (Forschungszentrum, Jülich, 2019).
- [48] E. Vitali, H. Shi, M. Qin, and S. Zhang, *Phys. Rev. B* **94**, 085140 (2016).
- [49] G. C. Wick, *Phys. Rev.* **80**, 268 (1950).
- [50] M. Suewattana, W. Purwanto, S. Zhang, H. Krakauer, and E. J. Walter, *Phys. Rev. B* **75**, 245123 (2007).
- [51] R. M. Martin, *Electronic Structure: Basic Theory and Practical Methods* (Cambridge University Press, Cambridge, UK, 2020).
- [52] H. Shi and S. Zhang, *J. Chem. Phys.* **154**, 024107 (2021).
- [53] J. Carlson, J. E. Gubernatis, G. Ortiz, and S. Zhang, *Phys. Rev. B* **59**, 12788 (1999).
- [54] H. Kwee, S. Zhang, and H. Krakauer, *Phys. Rev. Lett.* **100**, 126404 (2008).
- [55] M. Bernasconi, G. Chiarotti, P. Focher, S. Scandolo, E. Tosatti, and M. Parrinello, *J. Phys. Chem. Solids* **56**, 501 (1995).

- [56] F. D. Malone, A. Benali, M. A. Morales, M. Caffarel, P. R. C. Kent, and L. Shulenburger, *Phys. Rev. B* **102**, 161104(R) (2020).
- [57] F. D. Murnaghan, *Proc. Natl. Acad. Sci. USA* **30**, 244 (1944).
- [58] A. P. Bartók, R. Kondor, and G. Csányi, *Phys. Rev. B* **87**, 184115 (2013).
- [59] S. Chen and S. Zhang, *Nature Computational Science* **2**, 736 (2022).
- [60] S. Chen and S. Zhang, Accurate phonon spectrum computations with auxiliary-field quantum Monte Carlo (unpublished).
- [61] S. Chen, Y. Yang, M. A. Morales, and S. Zhang, Algorithm for branching and population control in correlated sampling (unpublished).
- [62] L. Kleinman and D. M. Bylander, *Phys. Rev. Lett.* **48**, 1425 (1982).